

Research Article

Electromagnetic Field Behavior in Dispersive Isotropic Negative Phase Velocity/Negative Refractive Index Guided Wave Structures Compatible with Millimeter-Wave Monolithic Integrated Circuits

Clifford M. Krowne¹ and Maurice Daniel²

¹ Microwave Technology Branch, Electronics Science and Technology Division, US Naval Research Laboratory, Washington, DC 20375-5347, USA

² Electronics Science and Technology Branch, Sensors and Technology Division, DCS Corporation, 1330 Braddock Place, Alexandria, VA 22314, USA

Received 8 February 2007; Accepted 26 June 2007

Recommended by Christian Brosseau

A microstrip configuration has been loaded with a dispersive isotropic left-handed medium (LHM) substrate and studied regarding its high frequency millimeter-wave behavior near 100 GHz. This has been accomplished using a full-wave integral-equation anisotropic Green's function code configured to run for isotropy. Never before seen electromagnetic field distributions are produced, unlike anything found in normal media devices, using this *ab initio* solver. These distributions are made in the cross-sectional dimension, with the field propagating in the perpendicular direction. It is discovered that the LHM distributions are so radically different from ordinary media used as a substrate that completely new electronic devices based upon the new physics become a real possibility. The distinctive dispersion diagram for the dispersive medium, consisting of unit cells with split ring resonator-rod combinations, is provided over the upper millimeter-wave frequency regime.

Copyright © 2007 C. M. Krowne and M. Daniel. This is an open access article distributed under the Creative Commons Attribution License, which permits unrestricted use, distribution, and reproduction in any medium, provided the original work is properly cited.

1. INTRODUCTION

Tremendous interest in the last few years has occurred with the experimental realization of macroscopic demonstrations of left-handed media, predicted or at least suggested in the literature several decades ago [1]. Attention has followed on the focusing characteristics and related issues of left-handed media (LHM), with appropriate arrangements to accomplish such behavior, as shown by literature publications [2–25]. But no attention has been directed toward what intrinsic left-handed media could do in propagating devices used in integrated circuit configurations. This is not to say that some work has not happened on applications using backward wave production or LHM properties in specialized microwave devices which rely on reduced dimension negative phase velocity behavior [26–34]. (Also see references contained in [35, 36] for other focusing and backward wave devices.) And much of that work has looked at macroscopic realizations, which may be amenable in the future, with current efforts

on metamaterials, to advancing microwave integrated circuit component technology utilizing left-handed media.

We are particularly interested here in new physical properties being the result of using material which is intrinsically left-handed, or also variously referred to in the literature as negative phase velocity material (NPVM or NPV) or negative refractive index material (NRIM or NIM). There may be substantial interest in understanding the effects of left-handed media in guided wave structures since advances in integrated circuit technology, passive components, control components, and active devices have increasingly been utilizing layers and arrangements of many differing materials. From heterostructures in active devices to complex materials like chiral, ferroelectric, and ferromagnetic materials, in passive and control components, this trend has been rising. Efforts on metamaterials are sure to further this trend.

A hint at the remarkably different field distributions has been disclosed recently using LHM substrates in guided wave devices [37]. Dispersion diagram description of the physics

is provided in [35], and this diagram shows the effect of the RHM/LHM interface seen in the cross-sectional view on the propagation normal to the cross-section. Bands of pure phase propagation and bands of evanescent propagation occur. Also, negative phase velocity behavior of the LHM interacts with the RHM to generate regions of both ordinary wave propagation as well as backward wave propagation in the negative phase velocity sense relative to the guided wave power flow. In [35], only the low end band is displayed in field distribution plots at 5 GHz. But the plots shown are instructive for the new physics they demonstrate: unusual field line or circulation characteristics for the electric or magnetic fields, startling intensity variation of the fields, counter intuitive charge arrangement on the guiding metal strip, and interesting visual display of opposed Poynting vectors in adjoining RHM and LHM regions for power flow down the device.

Attention to the new possibilities for electronic devices is given in [36, 38] when using LHM/NPV substrates. There, distributions up to 40 GHz are provided, somewhat over the beginning of the millimeter-wave frequency band. However, nowhere have we made available the remarkable field distributions found at the higher millimeter wavelengths, and so in this paper, we would like to show for the first time what the fields look like at nearly $10^{11} = 100$ GHz (we will actually draw our attention to $f = 80$ GHz as a starting point). A new technique that we have developed of lifting out the lower magnitude fields in order to visualize their directions in arrow distribution plots will be utilized here for the first time (Section 5). This is particularly important in distribution plots where the field magnitudes may vary over many orders of magnitude. A number of field distribution plotting methods will be employed in this paper: arrow plots based upon linear representation of the field magnitude, arrow plots for both electric and magnetic fields based upon scaled representation of the field magnitude, line plots showing electric field behavior emanating from the strip and off of it, line plots showing magnetic field behavior circulating around the guiding strip and off of it, and magnitude plots of both the electric and magnetic fields.

Sections 2 and 3 provide short discussions of left-handed material properties (Section 2) and Green's function technique (Section 3) used to solve the material physics/field problem. Once these preliminaries are out of the way, the eigenvalues and dispersion diagram (Section 4) and the field distributions (Section 5) are determined.

2. LEFT-HANDED MATERIAL CHARACTERISTICS

It is expected that the left-handed medium characteristic to alter the electromagnetic field based upon its new properties contained in its tensors describing permittivity and permeability will not only lead to new structures enlisting just this new material, but eventually allow the creation of multi-layered devices containing various substances including left-handed media. Here we report on the new physics associated with left-handed media in guided wave propagating structures which are applicable to microwave and millimeter-

wave integrated circuits, although the focus here is primarily on the millimeter-wave region. Here we address the use of the left-handed media with its general bianisotropic crystalline properties reduced to scalars, that is, with anisotropic permittivity $\bar{\bar{\epsilon}}$ tensor set equal to the isotropic permittivity value $\epsilon\bar{1}$, and anisotropic permeability $\bar{\bar{\mu}}$ tensor set equal to the isotropic permeability value $\mu\bar{1}$. Consideration of the anisotropic or bianisotropic crystalline case is examined elsewhere [39]. Suffice it to say here that just as in the case of optical or lower frequency focusing, isotropy is what allows proper organization of all the wave fronts (or rays in the geometric optics limit). But in a guided wave structure, what may be the most critical issue is the assumption of isotropy in many applications to allow arbitrary field contouring or sculpting, although it is now known that particular anisotropies can lead to remarkable field asymmetries of potential use in electronic devices [40]. Individual unit cell construction and repetitive cells in all directions can lead to isotropy, as well as materials with intrinsic isotropic crystalline properties. The scalar relative permittivity and permeability ϵ and μ seen in the literature have frequency dependences $\epsilon(\omega)$ and $\mu(\omega)$. Left-handed material is obtained when $\text{Re}[\epsilon(\omega)] < 0$ and $\text{Re}[\mu(\omega)] < 0$ simultaneously. Whether this is a narrow- or wideband phenomenon will not be addressed here, other than to note that there may be both metaobject construction as well as intrinsic material methods to adjust the bandwidth. There is every indication today that these two implementation categories may provide enough design possibilities to make such bandwidth adjustment realistic. So, whether one uses nonresonant objects, resonant objects, microscopic properties of crystals, or nanoscale materials, there is no reason to doubt that the frequency region $\Delta\omega$ over which the desired behavior occurs may be viewed as being subject to the choice of the physicist or engineer for some intended use.

So, in order to study what the field distributions would do for a LHM substrate in a certain configuration at a particular frequency, we need to set $\text{Re}[\epsilon(\omega)] = -\epsilon_r$ and $\text{Re}[\mu(\omega)] = -\mu_r$, where $\epsilon_r =$ real positive constant and $\mu_r =$ real positive constant. Fundamental mode is sought, which has an eigenvalue even as $\omega \rightarrow 0$ ($f \rightarrow 0$). This is the simplest problem one can solve for in our inhomogeneous boundary condition problem. Hope for obtaining wideband behavior is now supported by recent results showing that negative refraction can be obtained by using heterostructures of intrinsic crystals with negligible dispersion [39, 41–43]. The narrowest behavior occurs with resonant structures like split ring resonator-rod combinations. Even for these structures, which are characterizable by $\epsilon(\omega) = 1 - (\omega_{pe}^2 - \omega_{e0}^2)/(\omega^2 - \omega_{e0}^2 + i\omega L_\epsilon)$ and $\mu(\omega) = 1 - F\omega^2/(\omega^2 - \omega_{m0}^2 + i\omega L_\mu)$ (these forms are widely quoted in the literature, with, for example, the permeability being derivable from [44]), because ω_{pe} , ω_{e0} , and F are subject to the designer's control, one can always, for a desired setting for ϵ and μ at a particular frequency ω , solve the two equations implicit in these depictions for the three unknowns, with a rich multiplicity of solutions. Finally, photonic crystals which provide the negative refraction using ordinary RHM crystals with RHM inclusions, may have

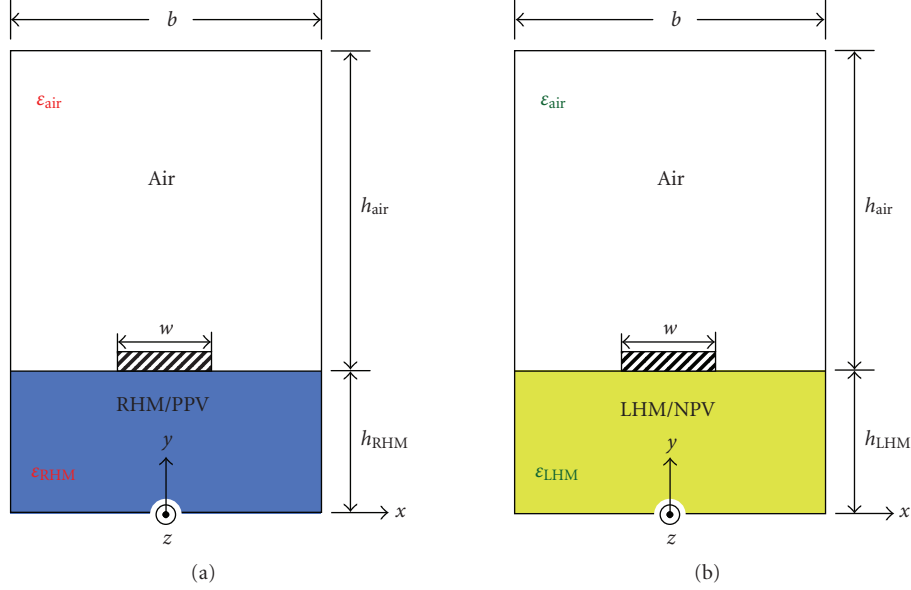


FIGURE 1: Cross-section of a microstrip structure with (a) a substrate using right-handed material (RHM/PPV) or (b) a substrate using left-handed material (LHM/NPV).

bandwidths somewhere between nondispersive and highly dispersive (as in the resonant structures).

3. GREEN'S FUNCTION FOR LEFT-HANDED GUIDED WAVE STRUCTURE

Green's function for the problem is a self-consistent one for a driving surface current vector Dirac delta function applied at the guiding microstrip metal, $\mathbf{J} = j_x \delta(x - x_0) \hat{x} + j_z \delta(x - x_0) \hat{z}$ with $x_0 = 0$ point on the strip. Figure 1(a) shows a cross-section of the structure with a right-handed material (RHM/PPV-ordinary material; PPV = positive phase velocity) used for the substrate, and Figure 1(b) shows a cross-section of the structure with a left-handed material (LHM/NPV). The Green's function is a dyadic, constructed as a 2×2 array relating tangential x - and z -components of surface current density to tangential electric field components. This function is used to solve for the propagation constant (see [45] for a recent use of this type of Green's function). Determination of the field components is done in a second stage of processing, which in effect creates a large rectangular Green's function array, of size 6×2 , in order to generate all electromagnetic field components, including those in the y -direction normal to the structure layers. The governing equation of the problem can be stated as

$$\frac{d\psi}{dy} = i\omega \mathbf{R} \psi, \quad \psi = [E_x \ E_z \ H_x \ H_z]^T, \quad (1)$$

where the system 4×4 matrix \mathbf{R} depends on the Green's function and on the physical properties of the materials. This equation gives the tangential transverse a field component variation (column vector ψ) perpendicular to the surface in the y -direction. Auxiliary equations give the two remaining field components, E_y and H_y .

The self-consistent problem is solved by expanding the surface currents on the guiding microstrip metal in the infinite expansions $J_x = \sum_{i=1}^{n_x} a_{xi} j_{xi}(x)$ and $J_z = \sum_{i=1}^{n_z} a_{zi} j_{zi}(x)$, and then requiring the determinant of the resulting system of equations to be zero. At this step of the problem, only the surface current basis functions $j_{xi}(x)$ and $j_{zi}(x)$ need to be provided and the complex propagation constant $\gamma = \alpha + j\beta$ is returned by the computer code. Of course, the summation limits n_x and n_z must be truncated at an appropriate value when convergence is acceptable.

Acquisition of the electromagnetic fields necessitates obtaining the basis function expansion coefficients a_{xi} and a_{zi} , explicitly constructing the actual driving surface current density on the microstrip metal, finding the resulting top or bottom boundary fields, and then utilizing operators to pull up or down through the structure layers, generating the electric and magnetic fields throughout in the process. The entire solution method uses the constraint that the vertical side walls of the device are perfect electric walls (perfect metallic conductors), which can be shown to discretize the eigenvalues in the x -direction. These are the Fourier transform variables for the spectral domain, and an infinite set of them forms a complete set for the problem. Only a finite number of them are used, with their maximum number being denoted by n .

4. DISPERSION DIAGRAMS OF LHM AND RHM DEVICES

To gain some idea of the general trend of the propagation constant, a dispersion diagram is graphed in Figure 2 for an ordinary medium substrate in the millimeter-wave frequency regime for a device with air above the substrate and right-handed medium (RHM/PPV, PPV) below the strip with $\text{Re}[\epsilon(\omega)] = \epsilon_r = 2.5$, and $\text{Re}[\mu(\omega)] = \mu_r = 2.3$, substrate

thickness $h_s = 0.5$ mm, microstrip width $w = 0.5$ mm, air region thickness $h_a = 5.0$ mm, and vertical wall separation $b = 5.0$ mm. Also, $\text{Im}[\varepsilon(\omega)] = \varepsilon_i = 0$ and $\text{Im}[\mu(\omega)] = \mu_i = 0$ making the medium lossless. (We also consider the microstrip metal lossless, although modifications for its loss can be made [45], as well as for medium loss in the substrate [45].) There are two γ roots possible for even symmetry of the J_z surface current component. They are mirror images of each other, with one corresponding to a z -directed wave and the other to a $-z$ -directed wave propagating in the reverse longitudinal direction. The figure only shows the positive going wave solution (solid yellow curve) for the fundamental mode, and we see that $\gamma = \alpha + j\beta = j\beta$, meaning that pure phase behavior occurs in the RHM/PPV structure. The dispersion diagram was produced with $n_x = n_z = 1$ and $n = 200$, although we have found solutions up to $n_x = n_z = 9$ and $n = 900$, with the change in the numerical value being in the fourth decimal place. Because we are putting our attention deep into the millimeter-wavelength regime, plots will be later done at frequency $f = 80$ GHz, which for the RHM/PPV structure has $\bar{\beta} = \beta/k_0 = 2.200$.

For a left-handed medium LHM/NPV substrate, instead of choosing $\text{Re}[\varepsilon(\omega)] = -\varepsilon_r = -2.5$, $\text{Re}[\mu(\omega)] = -\mu_r = -2.5$, and $\text{Im}[\varepsilon(\omega)] = -\varepsilon_i = 0$, $\text{Im}[\mu(\omega)] = -\mu_i = 0$ [35], with the geometric parameters being the same as for the RHM/PPV structure, we will consider a metamaterial model of the LHM/NPV substrate consisting of split ring resonators [44] with rods [46] (SRRs). Such a metamaterial will introduce explicit material dispersion into the problem, in addition to the dispersion already in the problem due to the guided configuration. For the rods, which we assume are continuous ($f_{e0} = 0$), their radius is chosen to be $r_e = 6.313 \mu\text{m}$, with a lattice spacing of $a = 0.690 \mu\text{m}$. These values are associated with an effective plasma frequency $f_{pe} = 149.67$ GHz and electric damping factor $L_e = 0.1305$ GHz (using aluminum). For the SRRs, the sheets' split on cylinder's model is used as an approximation to the split rings, with cylinder radius $r_m = 0.2761$ mm, and the concentric cylinder distance separation $d = 0.1668$ mm. Using the lattice spacing selected above yields $F = 0.5027$. These values are associated with a magnetic resonance frequency $f_{m0} = 74.03$ GHz, crossover frequency where effective permeability $\mu_{\text{eff}} = 0$ of $f_{mco} = 105$ GHz, and magnetic damping factor $L_\mu = 0.0853$ GHz (using aluminum). Thus, the dispersive material equations for the SRRs are completely determined:

$$\varepsilon(\omega) = 1 - \frac{\omega_{pe}^2 - \omega_{e0}^2}{\omega^2 - \omega_{e0}^2 + i\omega L_e} = 1 - \frac{\omega_{pe}^2}{\omega^2 + i\omega L_e}, \quad (2)$$

$$\mu(\omega) = 1 - \frac{F\omega^2}{\omega^2 - \omega_{m0}^2 + i\omega L_\mu}.$$

For the LHM/NPV structure, in the limiting case of $L_e \rightarrow 0$ and $L_\mu \rightarrow 0$, two γ solutions exist which have $\alpha = 0$, and $\bar{\beta} = \beta/k_0 = 1.177647$ and 1.786090 (quoted values for n_x and $n_z = 1$ and $n = 200$). One corresponds to a forward wave for nondispersive intrinsic LHMs ($\bar{\beta} = \beta/k_0 = 1.78609$), where the product of the integrated Poynting vector (net power through the cross section) and phase vector in the

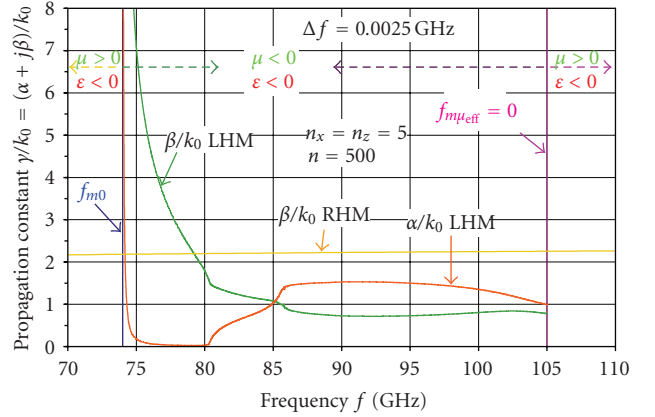


FIGURE 2: Complex propagation constant γ/k_0 versus frequency f over the range 70–105 GHz for the fundamental modes of an microstrip configuration for an RHM/PPV substrate and for a LHM/NPV substrate with SRR inclusions.

z -direction is $\oint \mathbf{P}_z \cdot \beta \hat{z} dA > 0$ (dA is the differential cross-sectional element) or equivalently $\mathbf{v}_{gl} \cdot \mathbf{v}_{pl} > 0$. The other solution is a backward wave for nondispersive intrinsic LHMs ($\bar{\beta} = \beta/k_0 = 1.177647$), where the product of the integrated Poynting vector and the phase vector in the z -direction is $\oint \mathbf{P}_z \cdot \beta \hat{z} dA < 0$ or equivalently $\mathbf{v}_{gl} \cdot \mathbf{v}_{pl} < 0$. Here, \mathbf{v}_{gl} and \mathbf{v}_{pl} are, respectively, the group and phase longitudinal velocities. These modes are referred to as fundamental modes in the sense that as $f \rightarrow 0$, a solution exists (we had earlier looked at this type of mode for the RHM/PPV substrate).

As damping loss is turned on and becomes finite, only the forward guided wave will exist, and the backward guided wave will cease to exist. The fundamental mode for the upper root is shown in Figure 2, not extending beyond either 74 GHz on the low end or 105 GHz on the high end because $\text{sg}[\varepsilon(\omega)] \text{sg}[\mu(\omega)] = -1$, and that product causes evanescent propagation to occur where β is extremely tiny. Below f_{m0} and above f_{mco} , $\mu > 0$ and $\varepsilon < 0$. However, between these critical frequency points, $\text{sg}[\varepsilon(\omega)] \text{sg}[\mu(\omega)] = +1$ and the wave propagates with $\mu < 0$ and $\varepsilon < 0$. Out of the range plotted, above the electric crossover frequency f_{eco} (near f_{pe} for low loss) where effective permeability $\varepsilon_{\text{eff}} = 0$, $\text{sg}[\varepsilon(\omega)] \text{sg}[\mu(\omega)] = +1$ will occur again, with $\mu > 0$ and $\varepsilon > 0$ this time, being completely reversed from the region between f_{m0} and f_{mco} .

The dispersion curves for the LHM/NPV substrate are plotted in Figure 2 using $n_x = n_z = 5$ and $n = 500$ with frequency increments of $\Delta f = 0.0025$ GHz between eigenvalue points (only small differences with solutions at $n_x = n_z = 9$, $n = 900$, $n_x = n_z = 1$, and $n = 100$ have been found, on the order of less than a few tenths of a percent). At 80 GHz, $\bar{\gamma} = (\bar{\alpha}, \bar{\beta}) = (0.0320222, 1.79365)$ for $n_x = n_z = 1$ and $n = 100$, whereas for $n_x = n_z = 9$ and $n = 900$, $\bar{\gamma} = (0.0322745, 1.79116)$. These values used the parameter settings mentioned above, except $L_e = 0.1305$ GHz and $L_\mu = 0.0853$ GHz, corresponding to about a fifty percent increase in loss width, providing a more conservative estimate of propagation loss due to the metamaterial which could occur

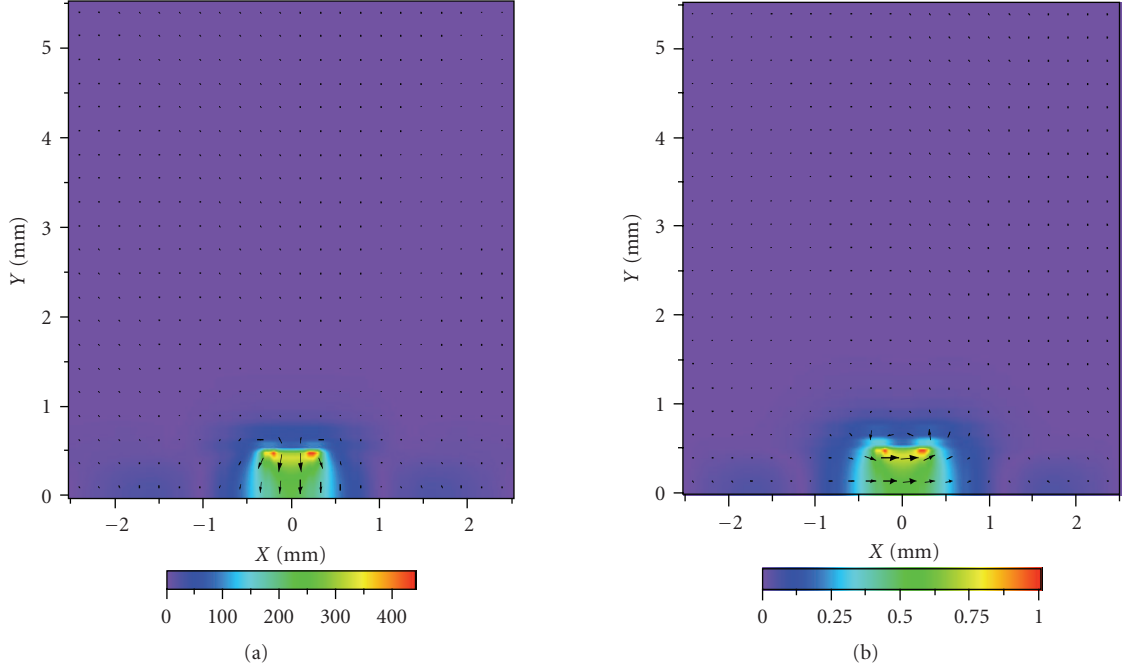


FIGURE 3: For an ordinary RHM/PPV substrate at 80 GHz, we have (a) electric field distributions in a color plot for magnitude E with an overlaid plot for vector \mathbf{E}_t in arrow form unscaled; (b) magnetic field distributions in a color plot for magnitude H with an overlaid plot for vector \mathbf{H}_t in arrow form unscaled.

from imperfect metal or lower conductivity metal. Permittivity and permeability at 80 GHz are $\epsilon = (-2.5156, 5.77348 \times 10^{-3})$ and $\mu = (-2.4817, 2.5713 \times 10^{-2})$, corresponding to loss tangents (ϵ_i/ϵ_r or μ_i/μ_r) of 2.28×10^{-3} and 1.04×10^{-2} . The reason why α rises and β falls after this frequency in Figure 2 is that both ϵ and μ are becoming ever more positive, providing much less left-handed material advantage, with the relative rates of change of ϵ and μ determining the details of the curves. Of course, once the frequency f_{mco} is hit, any effective propagation ceases.

5. ELECTROMAGNETIC FIELD DISTRIBUTIONS FOR LEFT-HANDED DEVICES

In order to correctly perceive the intensity of the fields, $E^2 = \sum_{i=1}^3 E_i^2 = E_x^2 + E_y^2 + E_z^2$ and $H^2 = \sum_{i=1}^3 H_i^2 = H_x^2 + H_y^2 + H_z^2$ are calculated and plotted as E and H using a color linear scale. These field magnitudes are related to the overall energy content when premultiplied by the appropriate dispersive permittivity and permeability derivatives [1, 47]—something that can be added to the model here by specifying additional microscopic physics of the LHM/NPV. This issue will be addressed in more detail elsewhere. What is important to realize here is that there is no conceptual difficulty in accomplishing that task. Care must be exercised in obtaining the linear color plot. Too small a grid results in a boxy appearance to the color distribution, making it very hard to interpret. Thus, we seek on the order of 10^4 grid points by partitioning each layer into 45 laminations and the vertical-to-vertical wall separation into 90 laminations, giving an 8372 grid points total

from the spectral domain code. (Calculations have been done with as many as 2.5×10^4 grid points.) A Fortner algorithm is used to produce the finished color plots [48].

5.1. RHM/PPV comparison structure

Once we have identified the $\bar{\beta}$ value and know the point in the diagram about which we wish to operate, we can proceed on to making a field distribution plot. Figures 3(a) and 3(b), respectively, show, for the comparison RHM/PPV structure, the E and H magnitude plots for $\bar{\beta} = \beta/k_0 = 2.200$, with unscaled linear arrow plots of electric vector \mathbf{E}_t and magnetic vector \mathbf{H}_t overlaid on them. (Surface current coefficients are $a_{x1} = (0, -0.0637503)$ and $a_{z1} = (1, 0)$.) The arrow overlays allow us to assess the actual cross-sectional magnitudes of the fields locally, as well as their directions, whereas the color distribution allows us to see continuously the entire magnitude of the fields. Field arrows are created in a $N \times M$ grid of points, $N \leq M$, usually $N = M - 1$, with $M = 22$ here. A number of basic features are seen in the plots. Variation of the magnitude has several periods in the x -direction associated with the effective wavelength in the RHM/PPV substrate. The electric field arrows emanating from the microstrip metal located about the device center line $x = 0$ mm, $y = 0.5$ mm, are directed out of the metal, consistent with a single charge residing on it, although it is in general nonuniformly distributed as expected for a conventional structure such as this. Magnetic field arrows circulate about the metal strip in one direction (Figure 3(b)), breaking up into extra fine structure below the interface, but those near the metal strip continue into the substrate just under the strip in regions of extremely

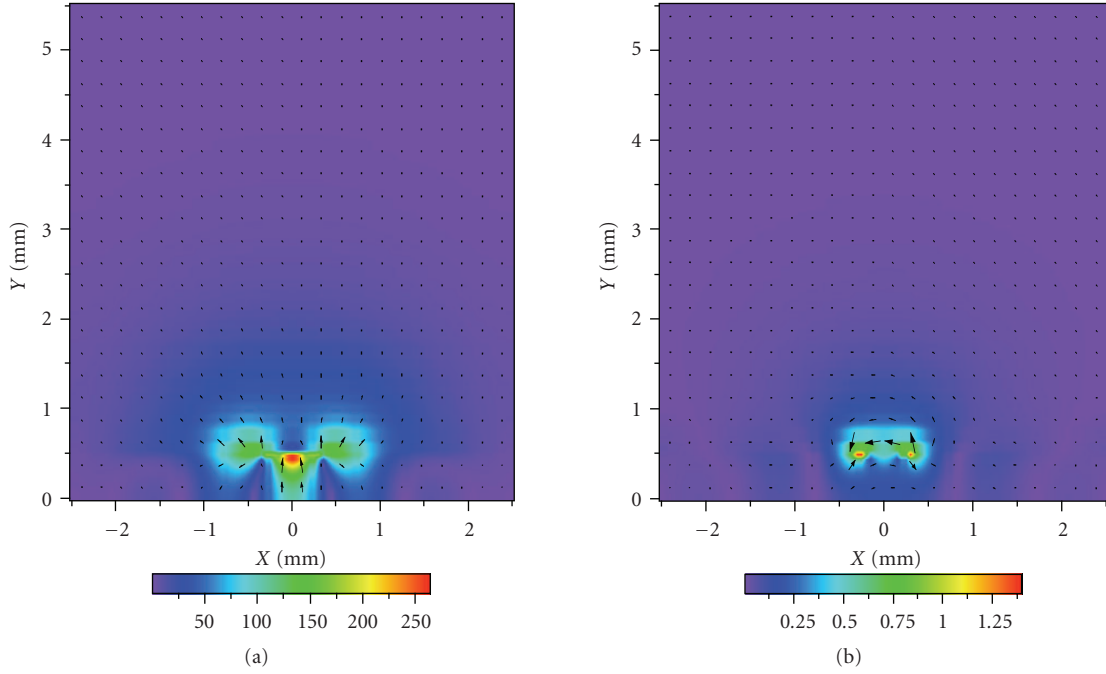


FIGURE 4: For an LHM/NPV substrate at 80 GHz, we have for the lower eigenvalue β (a) electric field distributions in a color plot for magnitude E with an overlaid plot for vector \mathbf{E}_t in arrow form unscaled; (b) magnetic field distributions in a color plot for magnitude H with an overlaid plot for vector \mathbf{H}_t in arrow form unscaled.

intense fields with singularities occurring based upon the edge condition. Even in the highly singular region near the metal strip which possesses delta function charge distributions near its edges, the discontinuity in the transverse \mathbf{H}_t field is related to the surface current \mathbf{J} to within 10% or better by the cross product $\mathbf{H}_t \times \hat{\mathbf{n}}$, where $\hat{\mathbf{n}} = \hat{\mathbf{y}}$ = normal to the interface. Outside of the metal strip interface region, field arrows crossing the interface obey the necessary boundary conditions from within a few percent to small fractions of a percent (these observations also hold for the LHM substrate case).

5.2. LHM/NPV structure

At $f = 80$ GHz for the LHM/NPV substrate case, Figures 4(a) and 4(b), respectively, show the electric E and magnetic H magnitude distributions for the lower root, backward wave LHM/NPV solution (valid for $L_\epsilon \rightarrow 0$, $L_\mu \rightarrow 0$), with unscaled linear arrow plots of electric vector \mathbf{E}_t and magnetic vector \mathbf{H}_t overlaid on them. (Surface current coefficients are $a_{x1} = (0, -0.128419)$ and $a_{z1} = (1, 0)$.) We see from these plots that the electric field E resides both around the guiding strip as well as under it in the LHM/NPV substrate. Magnetic field H is more localized near the strip metal. The upper forward wave LHM/NPV solution (valid for $L_\epsilon \neq 0$, $L_\mu \neq 0$) shown in Figures 5(a) and 5(b) demonstrates a more complicated distribution, with much more of it under the strip inside the LHM/NPV. (Surface current coefficients are $a_{x1} = (0, -0.142740)$ and $a_{z1} = (1, 0)$.) A number of striking differences are noted by comparing these results to

the ordinary substrate medium case in Figure 3 (RHM/PPV structure). Firstly, the E and H intensity distributions differ in appearance significantly for the LHM/NPV substrate structure compared to the relatively simple field pattern of the RHM/PPV structure. Secondly, in Figure 4(a), the electric field arrows \mathbf{E}_t do not point into (or out of) the metal strip but point roughly (this interpretation is modified by examining the field line distribution patterns to be discussed below in reference to Figure 6 for the LHM/NPV structure) in one direction above and below the strip, indicating that this branch still has a single charge (as was found for the RHM/PPV case in Figure 4) due to the reversed effect of the displacement electric field continuity condition normal to the interface. Thirdly, in Figure 4(a), electric field \mathbf{E}_t arrows, away from the metal strip near the interface, point in opposite directions as they cross the interface in terms of their normal components. Fourthly, in Figure 4(b), magnetic field \mathbf{H}_t arrows circulate around the strip in one direction above the interface and in the opposite direction below it, and the magnetic field arrows \mathbf{H}_t when crossing the interface point in opposite directions in terms of their y -components. Fifthly, in Figure 5(a), the electric field arrows \mathbf{E}_t point roughly (again this interpretation is modified later by the field line distribution patterns to be presented below in Figure 5) into (or out of) the metal guiding strip indicating a situation only possible if an infinitesimal dipolar charge arrangement exists in the vertical sense [35].

Of course, in addition to these noted differences between RHM/PPV and LHM/NPV substrates on guided wave behavior, the two solutions have significantly different field line

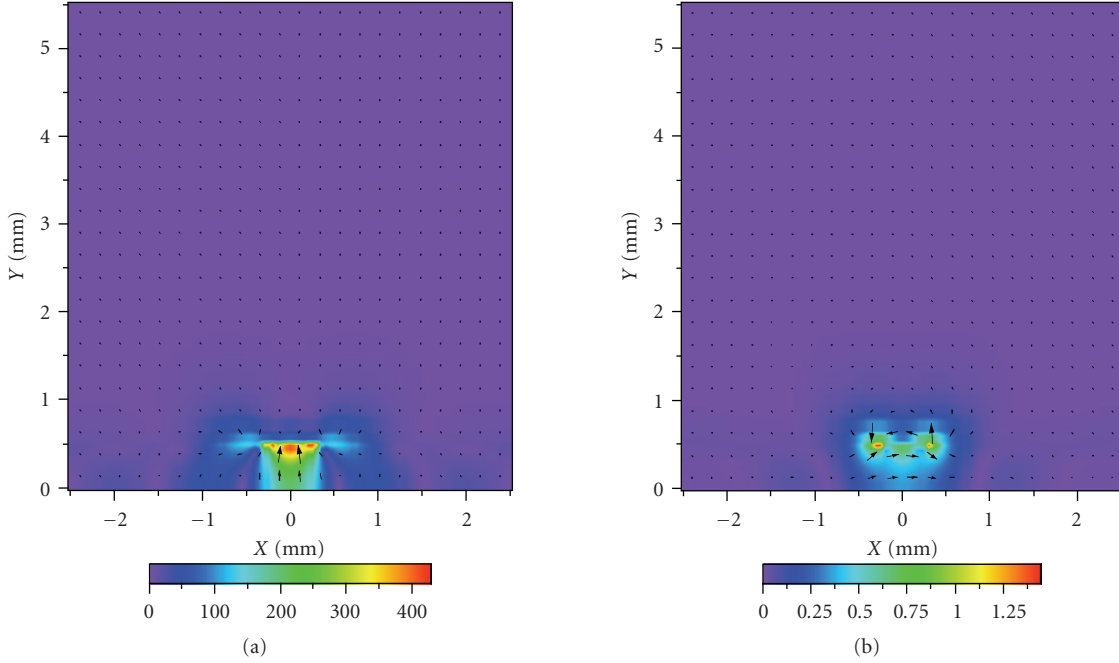


FIGURE 5: For an LHM/NPV substrate at 80 GHz, we have for the upper eigenvalue β (a) electric field distributions in a color plot for magnitude E with an overlaid plot for vector \mathbf{E}_t in arrow form unscaled; (b) magnetic field distributions in a color plot for magnitude H with an overlaid plot for vector \mathbf{H}_t in arrow form unscaled.

distribution patterns as seen in Figure 6 for the LHM/NPV structure. This is clear from the nearly circular circulating magnetic lines (first three) around the strip for the higher β value forward wave (see Figure 6(b)) compared to the broadly extended magnetic field lines for the lower β value backward wave (see Figure 6(a)). (This is evident by looking at the region above the substrate.) The electric field lines exhibit a dense pattern near the strip for the higher β value somewhat contained in a “shell,” compared to that of the lower β value mini-“shell” which barely shows this pattern emerging (examine the region just above the metal strip in the air zone). For the lower β value (see Figure 6(a)), there is a positive charge on the bottom half of the strip in the LHM/NPV (field lines enter into the strip) as well as on the ends (field lines exit from the last quarter length of the total strip length on either side of the strip) of the top part of the strip. But the mini-“shell” has its \mathbf{E}_t field lines emanating from the inner edges of the positive top charge at the boundary between this positive charge and an inside region of the top strip which is negatively charged. Upper β solution has its “shell” extending about 20% beyond the strip width, with the \mathbf{E}_t field lines emanating from the “shell” surface with the lines terminating nearest the strip center, originating near the intersection of the “shell” surface and the interface. Outside of the “shell” in both Figures 6(a) and 6(b), the electric field lines \mathbf{E}_t revert back to the simpler case of them seemingly to arise from a single uniform charge on both sides of the strip. Because the “shell” is not seen at considerably lower frequencies, this seems to imply that at higher frequencies the structure is trying to become more like an ordinary media layered

device. Finally, we note that both the electric \mathbf{E}_t and magnetic \mathbf{H}_t field line patterns are much more intricate for the higher β value in comparison to the lower β value beneath the interface in the LHM/NPV substrate.

To better visualize the directions of the fields throughout the device area, unconstrained by the need to follow selected field lines, but to retain those useful features in such field line plots, we have developed scaled arrow plots which lift the tiny magnitude field values from the background. One of the simplest methods to lift the fields in the background from numerical obscurity to visibility is to perform a log scaling such as

$$E_i = \begin{cases} \frac{E_i}{E_{i,\min}} \log_{10} \left(\left| \frac{E_i}{E_{i,\min}} \right| \right), & |E_i| > E_{i,\min}, \\ 0 & |E_i| \leq E_{i,\min}, \end{cases} \quad (3)$$

$$H_i = \begin{cases} \frac{H_i}{H_{i,\min}} \log_{10} \left(\left| \frac{H_i}{H_{i,\min}} \right| \right), & |H_i| > H_{i,\min}, \\ 0 & |H_i| \leq H_{i,\min}, \end{cases}$$

where $E_{i,\min}$ and $H_{i,\min}$ are positive magnitude cutoffs, and the argument presented to the \log_{10} operator is always positive whereas the sign of the field component is preserved in the prefactor. The problem with this scaling approach, though, is that it can damage the angle between the x - and

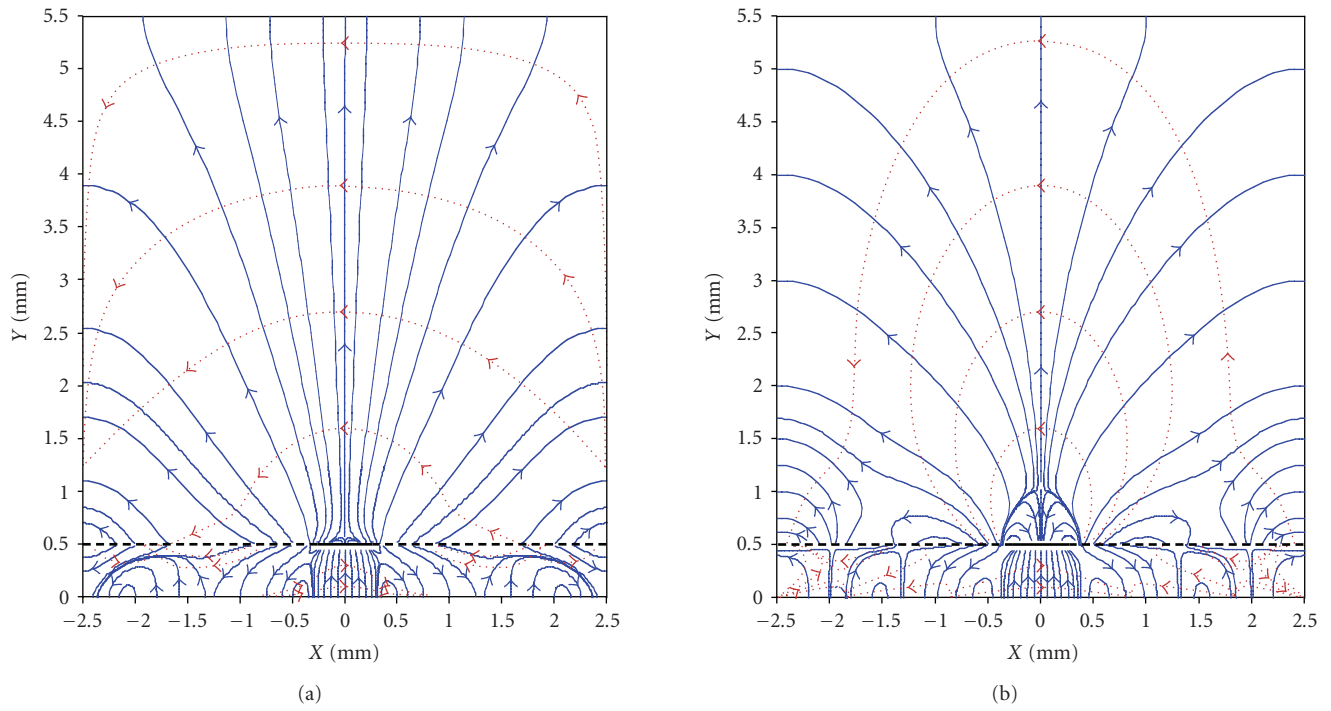


FIGURE 6: Electromagnetic field line distribution plots showing electric E_t (blue dotted line) and magnetic H_t (red dashed line) fields at 80 GHz for an LHM/NPV substrate in the fundamental mode for (a) the lower $\beta/k_0 = 1.177647$ and (b) the upper $\alpha/k_0 = 0.032022175$, $\beta/k_0 = 1.7936490$ eigenvalue solutions.

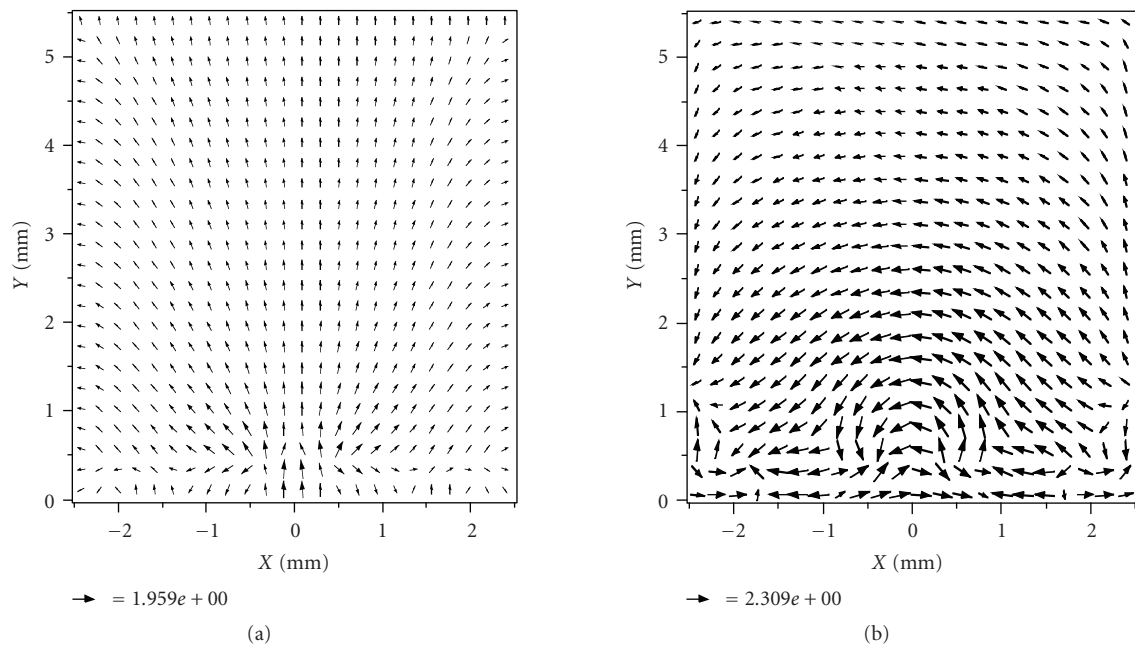


FIGURE 7: Arrow field distribution plots for the LHM/NPV structure at 80 GHz for (a) electric field E_t and (b) magnetic field H_t for the lower $\beta/k_0 = 1.1776$ eigenvalue solution using a trigonometric scaling method.

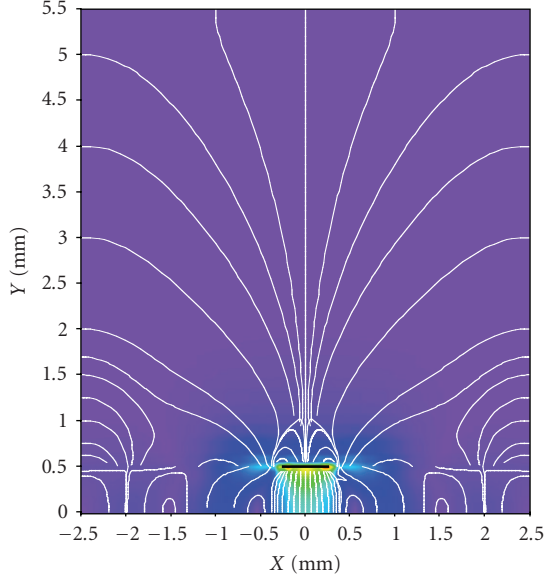


FIGURE 8: For an LHM/NPV substrate at 80 GHz, for the upper eigenvalue β , the electric field distribution in a color plot for magnitude E with an overlaid line distribution plot for E_t is shown.

y -components of the fields. Therefore, we have instead created an inverse trigonometric method,

$$\begin{aligned} E_i &= \frac{E_i}{E_t} \left[\left| \tan^{-1} \left(\frac{E_i}{E_{av}} \right) \right| + 0.75 \right], \\ H_i &= \frac{H_i}{H_t} \left[\left| \tan^{-1} \left(\frac{H_i}{H_{av}} \right) \right| + 0.75 \right]. \end{aligned} \quad (4)$$

Here,

$$\begin{aligned} E_t^2 &= E_x^2 + E_y^2, \\ H_t^2 &= H_x^2 + H_y^2. \end{aligned} \quad (5)$$

Ratio factor on the left is merely the cosine of the field angular offset from the x -axis, that is, $\cos \theta_E = E_i/E_t$ and $\cos \theta_H = H_i/H_t$. Figures 7(a) and 7(b), respectively, plot the electric and magnetic field distributions for the lower β LHM/NPV solution, with $E_{av} = 100$ V/m and $H_{av} = 0.01$ amps/m.

Lastly, in Figure 8 is provided the electric field E magnitude distribution for the LHM/NPV structure, overlaid with electric field lines E_t for the upper eigenvalue at 80 GHz. This figure combines some of the information from Figures 5(a) and 6(b), in such a way to assist visualization and understanding of the field behavior, allowing one to see the directional information at a glance while being able to assess the strength of the field.

6. CONCLUSION

In conclusion, we have shown completely new field distributions in a guided wave microstrip-like device structure containing left-handed material (LHM), otherwise referred to also as negative phase velocity material (NPV or NPVM)

in the power/phase sense. The results are valid for intrinsic LH crystalline materials, LH metamaterials, or LH heterostructure or layered crystalline materials. These field distributions show new physics, and although that is what has drawn our attention, such structures which are compatible with integrated circuit and solid state technology may open up many future possibilities. Unusual field distributions based upon new physics suggest the chance of completely new devices for future electronics besides the amendment of present devices which act as control components, active devices, and passive transmission structures. New devices could include millimeter-wave couplers, filters, phase shifters, isolators, and circulators, to mention a few.

We have also learned from the dispersion diagram for a SRR type of metamaterial LHM substrate that although the resonance nature of the unit cell can be extremely lossy at resonance, away from resonance there is a region of low enough loss to suggest realistic use in millimeter-wave integrated circuits.

REFERENCES

- [1] V. G. Veselago, "Electrodynamics of media with simultaneous negative electric permittivity and magnetic permeability," in *Advances in Electromagnetics of Complex Media and Metamaterials*, S. Zouhdi, A. H. Sihvola, and M. Arsalane, Eds., NATO Science, pp. 83–97, Kluwer Academic Publishers, Dordrecht, The Netherlands, 2002.
- [2] P. F. Loschialpo, D. L. Smith, D. W. Forester, F. J. Rachford, and J. Schelleng, "Electromagnetic waves focused by a negative-index planar lens," *Physical Review E*, vol. 67, no. 2, Article ID 025602, 4 pages, 2003.
- [3] F. J. Rachford, D. L. Smith, P. F. Loschialpo, and D. W. Forester, "Calculations and measurements of wire and/or split-ring negative index media," *Physical Review E*, vol. 66, no. 3, Article ID 036613, 5 pages, 2002.
- [4] W. T. Lu, J. B. Sokoloff, and S. Sridhar, "Refraction of electromagnetic energy for wave packets incident on a negative-index medium is always negative," *Physical Review E*, vol. 69, no. 2, Article ID 026604, 5 pages, 2004.
- [5] A. Lakhtakia and J. A. Sherwin, "Orthorhombic materials and perfect lenses," *International Journal of Infrared and Millimeter Waves*, vol. 24, no. 1, pp. 19–23, 2003.
- [6] A. Lakhtakia, "Handedness reversal of circular Bragg phenomenon due to negative real permittivity and permeability," *Optics Express*, vol. 11, no. 7, pp. 716–722, 2003.
- [7] R. B. Gregor, C. G. Parazzoli, K. Li, and M. H. Tanielian, "Origin of dissipative losses in negative index of refraction materials," *Applied Physics Letters*, vol. 82, no. 14, pp. 2356–2358, 2003.
- [8] S. Foteinopoulou, E. N. Economou, and C. M. Soukoulis, "Refraction in media with a negative refractive index," *Physical Review Letters*, vol. 90, no. 10, Article ID 107402, 4 pages, 2003.
- [9] D. R. Smith and D. Schurig, "Electromagnetic wave propagation in media with indefinite permittivity and permeability tensors," *Physical Review Letters*, vol. 90, no. 7, Article ID 077405, 4 pages, 2003.
- [10] A. A. Houck, J. B. Brock, and I. L. Chuang, "Experimental observations of a left-handed material that obeys Snell's law," *Physical Review Letters*, vol. 90, no. 13, Article ID 137401, 4 pages, 2003.

- [11] C. G. Parazzoli, R. B. Greigor, K. Li, B. E. C. Koltenbah, and M. Tanielian, "Experimental verification and simulation of negative index of refraction using Snell's law," *Physical Review Letters*, vol. 90, no. 10, Article ID 107401, 4 pages, 2003.
- [12] J. Pacheco Jr., T. M. Grzegorzczuk, B.-I. Wu, Y. Zhang, and J. A. Kong, "Power propagation in homogeneous isotropic frequency-dispersive left-handed media," *Physical Review Letters*, vol. 89, no. 25, Article ID 257401, 4 pages, 2002.
- [13] A. Lakhtakia, M. W. McCall, and W. S. Weiglhofer, "Brief overview of recent developments on negative phase-velocity mediums (alias left-handed materials)," *AEU—International Journal of Electronics and Communications*, vol. 56, no. 6, pp. 407–410, 2002.
- [14] R. Ruppin, "Surface polaritons of a left-handed material slab," *Journal of Physics Condensed Matter*, vol. 13, no. 9, pp. 1811–1818, 2001.
- [15] G. W. 't Hooft, "Comment on 'negative refraction makes a perfect lens'" *Physical Review Letters*, vol. 87, no. 24, Article ID 249701, 1 pages, 2001.
- [16] J. Pendry, "Pendry replies," *Physical Review Letters*, vol. 87, no. 24, Article ID 249702, 1 pages, 2001.
- [17] J. M. Williams, "Some problems with negative refraction," *Physical Review Letters*, vol. 87, no. 24, Article ID 249703, 1 pages, 2001.
- [18] J. Pendry, "Pendry replies," *Physical Review Letters*, vol. 87, no. 24, Article ID 249704, 1 pages, 2001.
- [19] G. Dewar, "Candidates for $\mu < 0$, $\epsilon < 0$ nanostructures," *International Journal of Modern Physics B*, vol. 15, no. 24–25, pp. 3258–3265, 2001.
- [20] Z. M. Zhang and C. J. Fu, "Unusual photon tunneling in the presence of a layer with a negative refractive index," *Applied Physics Letters*, vol. 80, no. 6, pp. 1097–1099, 2002.
- [21] A. Lakhtakia, "On perfect lenses and nihility," *International Journal of Infrared and Millimeter Waves*, vol. 23, no. 3, pp. 339–343, 2002.
- [22] E. Shamonina, V. A. Kalinin, K. H. Ringhofer, and L. Solymar, "Imaging, compression and Poynting vector streamlines for negative permittivity materials," *Electronics Letters*, vol. 37, no. 20, pp. 1243–1244, 2001.
- [23] J. Paul, C. Christopoulos, and D. W. P. Thomas, "Time-domain modelling of negative refractive index material," *Electronics Letters*, vol. 37, no. 14, pp. 912–913, 2001.
- [24] T. Weiland, R. Schuhmann, R. B. Greigor, et al., "Ab initio numerical simulation of left-handed metamaterials: comparison of calculations and experiments," *Journal of Applied Physics*, vol. 90, no. 10, pp. 5419–5424, 2001.
- [25] C. Caloz, C.-C. Chang, and T. Itoh, "Full-wave verification of the fundamental properties of left-handed materials in waveguide configurations," *Journal of Applied Physics*, vol. 90, no. 11, pp. 5483–5486, 2001.
- [26] A. Grbic and G. V. Eleftheriades, "Dispersion analysis of a microstrip-based negative refractive index periodic structure," *IEEE Microwave and Wireless Components Letters*, vol. 13, no. 4, pp. 155–157, 2003.
- [27] G. V. Eleftheriades, A. K. Iyer, and P. C. Kremer, "Planar negative refractive index media using periodically L-C loaded transmission lines," *IEEE Transactions on Microwave Theory and Techniques*, vol. 50, no. 12, pp. 2702–2712, 2002.
- [28] A. Grbic and G. V. Eleftheriades, "Experimental verification of backward-wave radiation from a negative refractive index metamaterial," *Journal of Applied Physics*, vol. 92, no. 10, pp. 5930–5935, 2002.
- [29] A. Alu and N. Engheta, "Radiation from a traveling-wave current sheet at the interface between a conventional material and a metamaterial with negative permittivity and permeability," *Microwave and Optical Technology Letters*, vol. 35, no. 6, pp. 460–463, 2002.
- [30] N. Engheta, "An idea for thin subwavelength cavity resonators using metamaterials with negative permittivity and permeability," *IEEE Antennas and Wireless Propagation Letters*, vol. 1, no. 1, pp. 10–13, 2002.
- [31] C. Caloz, A. Sanada, L. Liu, and T. Itoh, "A broadband left-handed (LH) coupled-line backward coupler with arbitrary coupling level," in *IEEE MTT-S International Microwave Symposium Digest*, vol. 1, pp. 317–320, Philadelphia, Pa, USA, June 2003.
- [32] I.-H. Lin, C. Caloz, and T. Itoh, "A branch-line coupler with two arbitrary operating frequencies using left-handed transmission lines," in *IEEE MTT-S International Microwave Symposium Digest*, vol. 1, pp. 325–328, Philadelphia, Pa, USA, June 2003.
- [33] H. Okabe, C. Caloz, and T. Itoh, "A compact enhanced-bandwidth hybrid ring using a left-handed transmission line section," in *IEEE MTT-S International Microwave Symposium Digest*, vol. 1, pp. 329–332, Philadelphia, Pa, USA, June 2003.
- [34] N. Engheta, "Ideas for potential applications of metamaterials with negative permittivity and permeability," in *Advances in Electromagnetics of Complex Media and Metamaterials*, S. Zouhdi, A. H. Sihvola, and M. Arsalane, Eds., NATO Science, pp. 19–37, Kluwer Academic Publishers, Dordrecht, The Netherlands, 2002.
- [35] C. M. Krowne, "Physics of propagation in left-handed guided wave structures at microwave and millimeter wave frequencies," *Physical Review Letters*, vol. 92, no. 5, Article ID 053901, 4 pages, 2004.
- [36] C. M. Krowne and M. Daniel, "Electronic aspects of propagation in left-handed guided wave structures: electromagnetic-media interactions," in *IEEE MTT-S International Microwave Symposium Digest*, vol. 1, pp. 309–312, Philadelphia, Pa, USA, June 2003.
- [37] C. M. Krowne, "Physics and electronics of left-handed guided wave devices," *Bulletin of the American Physical Society*, vol. 48, part 1, p. 580, 2003.
- [38] C. M. Krowne, "Electromagnetic-field theory and numerically generated results for propagation in left-handed guided-wave single-microstrip structures," *IEEE Transactions on Microwave Theory and Techniques*, vol. 51, no. 12, pp. 2269–2283, 2003.
- [39] C. M. Krowne, "Negative refractive Bi—crystal with broken symmetry leading to unusual fields in guided wave heterostructures," *Bulletin of the American Physical Society*, vol. 49, part 2, p. 928, 2004.
- [40] C. M. Krowne, "Left-handed material anisotropy effect on guided wave electromagnetic fields," *Journal of Applied Physics*, vol. 99, no. 4, Article ID 044914, 19 pages, 2006.
- [41] Y. Zhang, B. Fluegel, and A. Mascarenhas, "Total negative refraction in real crystals for ballistic electrons and light," *Physical Review Letters*, vol. 91, no. 15, Article ID 157404, 4 pages, 2003.
- [42] C. M. Krowne, "Negative-refractive bicrystal with broken symmetry produces asymmetric electromagnetic fields in guided-wave heterostructures," *Physical Review Letters*, vol. 93, no. 5, Article ID 053902, 2004.
- [43] A. Lakhtakia and C. M. Krowne, "Restricted equivalence of paired epsilon-negative and mu-negative layers to a negative

- phase-velocity material (alias left-handed material),” *Optik*, vol. 114, no. 7, pp. 305–307, 2003.
- [44] J. B. Pendry, A. J. Holden, D. J. Robbins, and W. J. Stewart, “Magnetism from conductors and enhanced nonlinear phenomena,” *IEEE Transactions on Microwave Theory and Techniques*, vol. 47, no. 11, pp. 2075–2084, 1999.
- [45] C. M. Krowne, “Dyadic Green’s function modifications for obtaining attenuation in microstrip transmission layered structures with complex media,” *IEEE Transactions on Microwave Theory and Techniques*, vol. 50, no. 1, pp. 112–122, 2002.
- [46] J. B. Pendry, A. J. Holden, W. J. Stewart, and I. Youngs, “Extremely low frequency plasmons in metallic mesostructures,” *Physical Review Letters*, vol. 76, no. 25, pp. 4773–4776, 1996.
- [47] L. D. Landau, E. M. Lifshitz, and L. P. Pitaevskii, *Electrodynamics of Continuous Media*, Pergamon Press, Oxford, UK, 1984.
- [48] Fortner Research LLC. Commercial plotting software, 1996.



Hindawi

Submit your manuscripts at
<http://www.hindawi.com>

